

Review

Recent Progress of Squaraine-Based Fluorescent Materials and Their Biomedical Applications

Weiguo Qiao and Zhong'an Li * 

Key Laboratory for Material Chemistry of Energy Conversion and Storage, Ministry of Education, School of Chemistry and Chemical Engineering, Huazhong University of Science and Technology, Wuhan 430074, China; qiaowg@hust.edu.cn

* Correspondence: lizha@hust.edu.cn

Abstract: Squaraines (SQs) are unusual cyanine dyes with a unique resonance-stabilized zwitterionic structure. These dyes have attracted significant attention in the fields of organic electronics and organic photonics, due to their facile synthesis, intense and narrow visible and near-infrared absorption/emission, high photostability, low biotoxicity, etc. In this review, we summarize the recent progress of SQ-based fluorescent materials and their biomedical applications. After a brief introduction to SQs, general synthetic routes and design principles of SQ-based fluorescent materials, as well as their aggregation-induced luminescence behaviors, are discussed. Subsequently, their biomedical applications for cell imaging and as fluorescent sensors and therapeutic agents are introduced. Finally, a summary and perspective are given for promoting the development of SQs-based fluorescent materials.

Keywords: squaraine dyes; fluorescence; sensors; bioimaging; phototherapy



Citation: Qiao, W.; Li, Z. Recent Progress of Squaraine-Based Fluorescent Materials and Their Biomedical Applications. *Symmetry* **2022**, *14*, 966. <https://doi.org/10.3390/sym14050966>

Academic Editor: Maria Sameiro T. Gonçalves

Received: 23 March 2022

Accepted: 3 May 2022

Published: 9 May 2022

Publisher's Note: MDPI stays neutral with regard to jurisdictional claims in published maps and institutional affiliations.

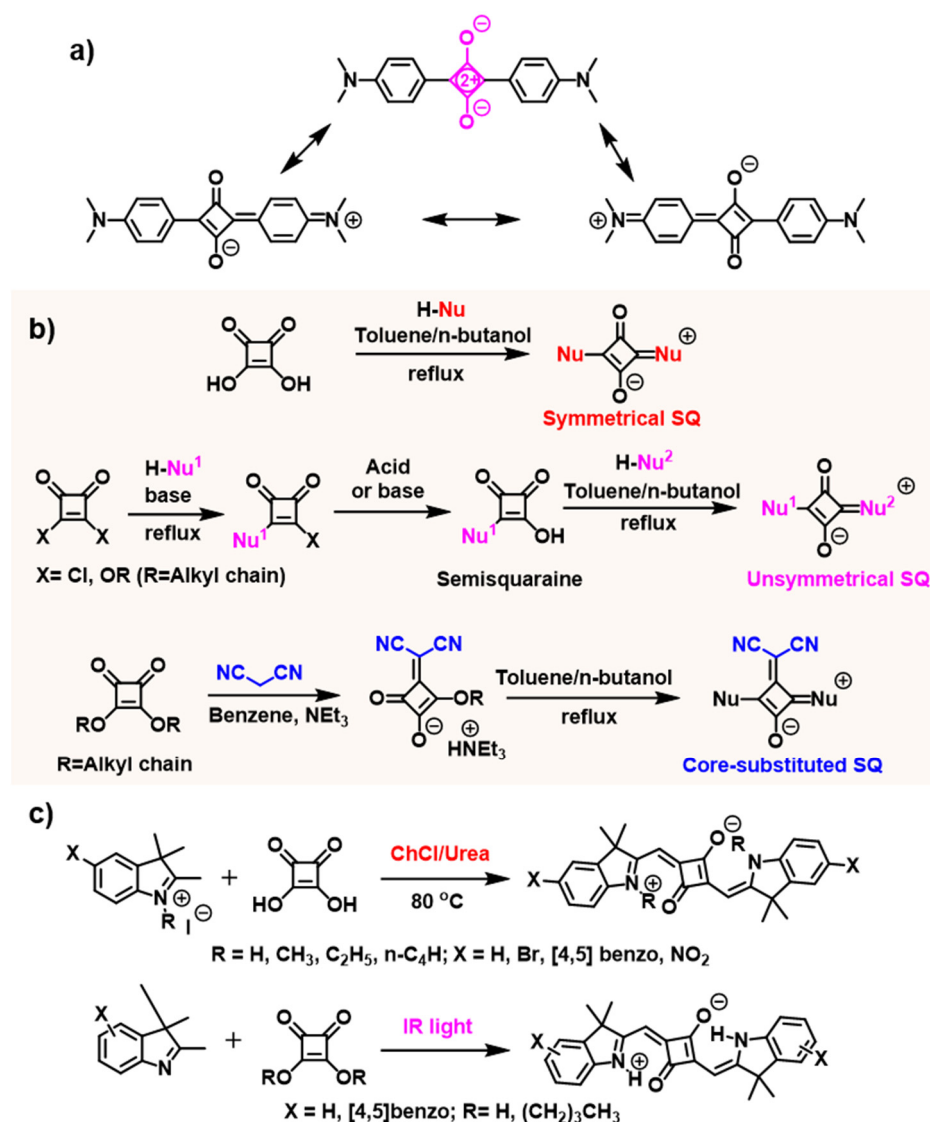


Copyright: © 2022 by the authors. Licensee MDPI, Basel, Switzerland. This article is an open access article distributed under the terms and conditions of the Creative Commons Attribution (CC BY) license (<https://creativecommons.org/licenses/by/4.0/>).

1. Introduction

In recent years, organic dyes have been widely used in the fields of organic light-emitting diodes, organic photovoltaics, sensing, biological imaging, theragnostic, etc. [1–3], due to their attractive advantages, including facile synthesis, low cost, easily tunable chemical structures and properties, good biocompatibility, and so on [4–6]. Among them, cyanine dyes have attracted significant attention from researchers attributed to their favorable optical properties, including narrow absorption/emission band with broad spectral range, large molar extinction coefficient, high emission efficiency, and so on [7,8]. A cyanine generally consists of a conjugated polymethine chain with an odd number of methine units, and possesses a highly delocalized charge along the chain. Thus, an attractive feature of cyanines is that their optical properties are highly correlated with the polymethine chain length.

Squaraine dyes (SQs) are a peculiar class of cyanine dyes. One of the biggest structure differences between SQs and other types of cyanine dyes is that SQs contain an electron-deficient square ring at the center of the polymethine chain, leading to a quadrupolar donor-acceptor-donor (D-A-D) structure with a unique resonance-stabilized zwitterionic feature, as shown in Scheme 1a [9–13]. In addition, the central square ring can make the polymethine chain rigid and planar to resist the photoisomerization and oxidation, and thus SQs intrinsically exhibit a greater stability over other cyanines [14,15]. The first example of an SQ, derived from squaric acid, was reported by Triebs and Jacob in 1965 [16]. Subsequently, numerous SQs have been reported by researchers using different electron-rich subunits, such as pyrroles, indolenines, quinolines, benzothiazoles, *N*, *N*-dialkylanilines and phenols, etc., which have been widely used as photosensitizers for photovoltaics, organic semiconductors, nonlinear optical materials, and so on [4,17–21].



Scheme 1. (a) Resonance-stabilized zwitterionic structure of a representative SQ. (b) Conventional synthetic pathways of symmetrical, unsymmetrical, and core-substituted SQs. (c) New synthetic pathways of symmetrical SQs.

SQs can be simply divided into symmetrical SQs and unsymmetrical SQs, depending on whether the end-groups are the same. Their synthetic routes are shown in Scheme 1b [20,22]. As shown, the symmetrical SQ is simply synthesized by the condensation of one equivalent squaric acid with two equivalent nucleophiles in a mixture of high-boiling-point alcohol and aromatic hydrocarbons. Although the major product is the 1,3-substituted SQ, the 1,2-substituted by-product can also be observed [23]. Unlike symmetrical SQs, the synthesis of unsymmetrical SQs is less straightforward, and it usually involves three steps: (1) one equivalent nucleophile is used to react with squaryl dichloride or squaric acid ester to give a stable intermediate, (2) the intermediate is treated with base or acid to afford the semisquaraine, (3) the semisquaraine reacted with another equivalent nucleophile. However, combining different end-groups allows for a better tuning of the chemical and optical properties of unsymmetrical dyes. Moreover, the core-substituted SQs mean that one oxygen atom of the central square ring is replaced by other groups (Scheme 1b), among which the dicyanomethylene group is the most efficient electron-withdrawing substituent to modify the molecular geometry, molecular crystallinity, and the optical properties [24,25]. Recently, scientists have also turned their attention to new synthetic approaches towards SQs. For example, Shankarling et al. developed a more

environment-friendly approach to obtaining symmetrical SQs with enhanced yield by using choline chloride/urea mixtures as the biorenewable deep eutectic solvent (Scheme 1c) [26]. Furthermore, a solvent-free infrared radiation synthetic method has been reported by Punzi et al. for preparing indolenine-based SQs (Scheme 1c) [27].

SQs have been successfully explored as fluorescent sensors and bioimaging agents. The fluorescence sensing is, for example, achieved by introducing a specific recognition site [28]. Additionally, SQs display aggregation properties that are susceptible to various external factors, such as ions, pH, protein etc. Changing the aggregation behavior is generally accompanied by a change in the optical response [29]. Furthermore, SQs with efficient non-radiative transition and singlet oxygen- ($^1\text{O}_2$) generation efficiency have been reported as photodynamic therapy (PDT) and photothermal therapy (PTT) agents. The corresponding photophysical mechanisms for PDT and PTT are explained using the Jablonski diagram (Figure 1) [30,31]. As shown, the electrons are excited under suitable excitation, and the direct radiative decay to the ground state (S_0) is fluorescence, which is suitable for bioimaging, while the nonradiative vibration relaxation to S_0 is always accompanied by heat generation, which thus is applied to PTT. For PDT, the excitons at the lowest triplet excited state (T_1) could be transferred to the nearby substrates, such as oxygen, leading to the generation of toxic reactive oxygen species (ROS) to kill the surrounding cancer cells. Generally, ROS are divided into two categories: (1) Type I photosensitizers are obtained when T_1 reacts with the biological molecules to form $\bullet\text{OH}$, $\text{O}_2^{\bullet-}$, and H_2O_2 by electron transfer process; (2) Type II photosensitizers are obtained when T_1 transfers energy to the ground state oxygen to form $^1\text{O}_2$ by energy transfer process. By adjusting the molecular structures, a variety of SQ-based fluorescent materials have been developed for different applications. In this review, we summarize the recent progress of SQs for their applications in the detection of specific analytes, bioimaging, and therapeutics, and we also discuss the challenges and perspectives of future design of SQs.

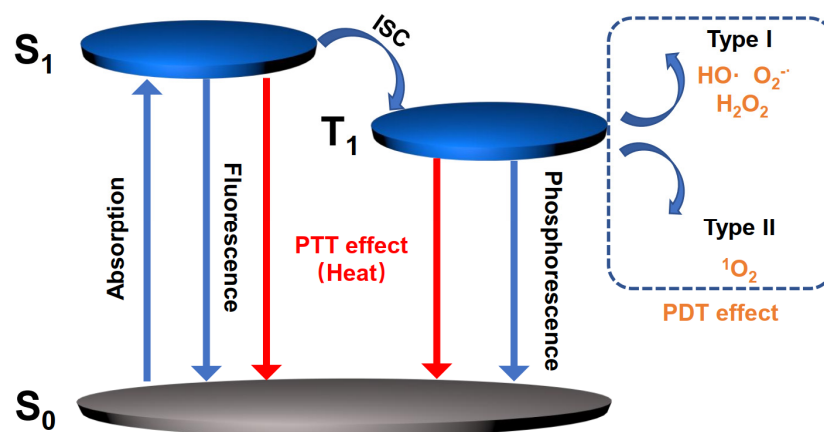


Figure 1. Simplified schematic of a Jablonski diagram.

2. New Design Strategies of SQ-Based Fluorescent Materials

Although SQs show favorable optical properties, a long-standing challenge for limiting SQ-based luminogens is the undesired aggregation causes quenching (ACQ) effect. This always occurs in their aggregate state, i.e., in aqueous solution, caused by strong intermolecular interactions as a result of their highly planar and quadrupolar structure [29]. To solve this problem, researchers have recently made great efforts to explore new design strategies by carefully tuning the end-groups, which has, encouragingly, led to attractive crystallization-induced emission enhancement (CIEE) [32] and aggregation induced emission (AIE) [33]. The CIEE and AIE properties of SQs are mainly attributed to the control of their self-assembly as well as the mitigation of tight π - π stacking through rotor structures.

2.1. SQs with CIEE Properties

Unsymmetrical SQs have constituted a large portion of SQ-based fluorescent materials. This is because compared to the symmetrical structure, unsymmetrical SQs exhibit much better flexibility for synthetic manipulation, making their absorption and emission properties easily tunable by modifying the end-groups [10]. More importantly, symmetry breaking can to some degree weaken the strong intermolecular interactions between SQs. For example, Gao et al. developed two piperidine-capped unsymmetrical SQs, i.e., NCSQ-g and CCSQ-1, as shown in Figure 2a [34]. NCSQ-g was found to show unconventional solid-state fluorescence (photo-luminescence quantum yield, $\Phi_{\text{PLQY}} = 0.36$), while CCSQ-1 only had intense fluorescence in solution, associated with a typical ACQ effect in the solid state (Figure 2b). Interestingly, as shown in Figure 2c, the emission spectrum of the NCSQ-g powders exhibited an almost complete overlap with the absorption band of CCSQ-1 in solution, enabling an efficient energy transfer from NCSQ-g powder to CCSQ-1. When a very small amount (0.0001–1.0 mol%) of CCSQ-1 was doped into NCSQ-g, the characteristic emission peak of NCSQ-g at 548 nm gradually decreased, while the emission of CCSQ-1 appeared and gradually increased with increasing amounts of CCSQ-1. As a result, various fluorescence colors from yellow-green to scarlet was obtained, as shown in Figure 2d, by doping a small amount of CCSQ-1 powder into NCSQ-g (0–0.5 mol%).

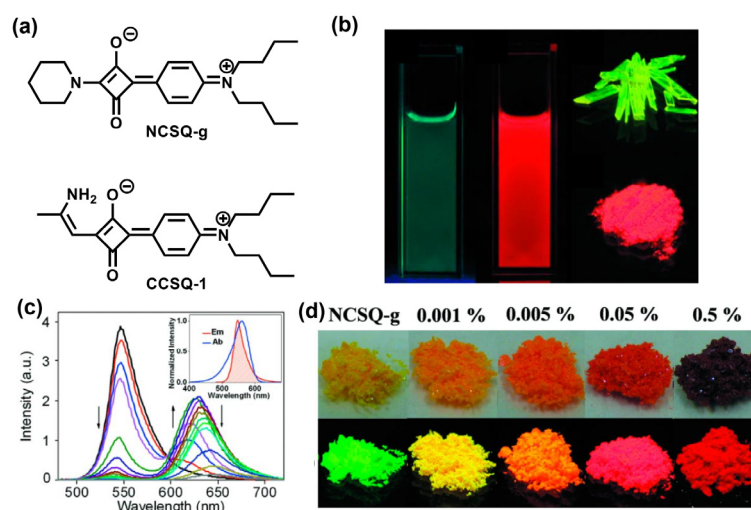


Figure 2. (a) Molecular structures of NCSQ-g and CCSQ-1. (b) Photographs of NCSQ-g (green) and CCSQ-1 (red) in THF solution (left) and photographs of crystals of NCSQ-g (green) and the CCSQ-1-doped NCSQ-g crystal powder (0.05 mol%, red) (right) under UV lamp illumination. (c) Fluorescent spectra of CCSQ-1/NCSQ-g crystalline at different ratios of NCSQ-g. Inset: the spectral overlap of the crystal emission of NCSQ-g (red) and the absorption of CCSQ-1 in THF solution (blue). (d) Photographs of the CCSQ-1-doped NCSQ-g crystalline (0, 0.001, 0.005, 0.05, and 0.5 mol%) under daylight (top) and UV lamp illumination (bottom). Reprinted with permission from Ref. [34]. Copyright 2012, American Chemical Society.

On the basis of the work of NCSQ-g, Gu and Peng et al. recently reported another piperidine-capped unsymmetrical SQ named CIEE-SQ, produced by changing the length of the alkyl chain of aniline end group (Figure 3a) [35]. CIEE-SQ exhibited no emission in diluted THF solution, but strong yellow emission in crystal (Figure 3b), suggesting crystallization-induced emission reverses from dark states to bright excited states. Meanwhile, the CIEE-SQ-CHCl₃ co-crystal (Figure 3c) was obtained in CHCl₃ solution with the yellow-green emission. Moreover, as shown in Figure 3d, the study demonstrated that when the filter paper strip immobilized with CIEE-SQ was put into the vessel with the saturated CHCl₃ vapor, intense yellow-green emission was observed under 365 nm UV lamp, reverting to a weak orange-yellow emission after removal from vessel. This phenomenon can be repeated many times without apparent fatigue (Figure 3e). On this

basis, a simple encryption model was established; the strong yellow-green emission of the character of “C” encrypted by CIEE-SQ was only illuminated by CHCl_3 fuming under UV irradiation while other characters showed no emission (Figure 3f).

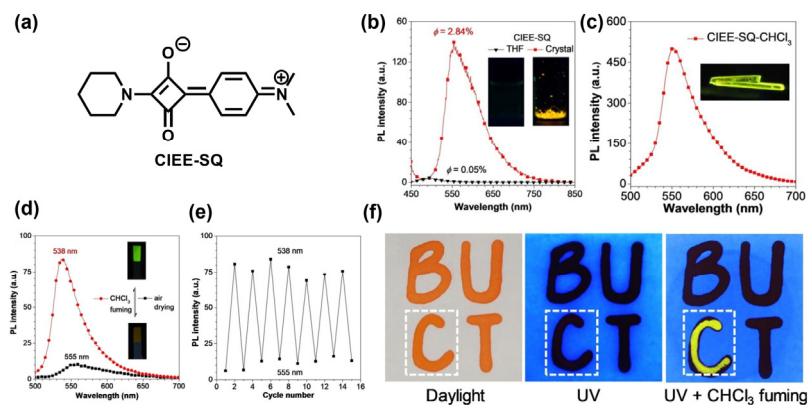


Figure 3. (a) Molecular structure of CIEE-SQ. (b) Fluorescent spectra and photos (inset) of CIEE-SQ in THF solution and crystal state. (c) Fluorescent spectrum of CIEE-SQ- CHCl_3 co-crystal. Inset: fluorescent photograph taken by UV lamp illumination. (d) Fluorescent spectra of filter papers before and after fuming by CHCl_3 vapor. Inset: fluorescent images with CHCl_3 fuming and air drying under UV lamp illumination. (e) The recycle of fluorescent intensities before and after fuming with CHCl_3 vapor for filter papers. (f) Data encryption and decryption on a filter paper based on CIEE-SQ. Reprinted with permission from Ref. [35]. Copyright 2020, Wiley-VCH.

In contrast to the commonly explored 1,3-substituted unsymmetrical SQs, 1,2-substituted unsymmetrical SQs exhibit more distorted molecular structure, but greater fluorescent emission properties. Wang et al. reported two novel 1,2-unsymmetrical SQs, namely SQM and SQB (Figure 4a), using benzimidazole derivatives modified with methyl and benzyl groups as the end groups, respectively [36]. Therein, the benzimidazole derivatives provided a torsion angle with respect to the central squarate ring to suppress the intense π - π stacking. As is depicted in Figure 4b, the single crystals of SQM and SQB were obtained from different solvents with strong bright yellow to red fluorescence. In crystal, the SQM molecules self-assembled into 1D microrods, whereas 1D microrods (Z -SQB- CH_2Cl_2) or 2D microplates (E -SQB- $2\text{CH}_3\text{OH}$) were found for the SQB assemblies. In Figure 4c, upon subjecting the red-emitting E -SQB- CH_3OH crystalline to various solvent vapors, quite distinct emission colors can be identified. Moreover, the multiple vapochromism of the SQB-solvent assemblies were demonstrated in Figure 4d, indicating that crystalline SQB can be used as a potential fluorescent sensor for the detection of different organic solvent vapors.

Recently, symmetrical SQs have also been successfully designed to achieve CIEE properties. For example, Gu et al. synthesized a symmetrical SQ based on bis(4-chlorophenyl) amine end group (SPOC-SQ), which can form emission-tunable, purely organic, soft porous crystals (Figure 5a) [37]. The formation of porous crystal framework is promoted by intermolecular interactions, including π - π interactions and H-bonds. SPOC-SQ performed weak emission in solution state, but efficient green emission in single crystal state, thus exhibiting CIEE properties. Interestingly, these crystals were found to exhibit reversible stimuli-responsive single-crystal-to-single-crystal (SCSC) structural transformation, accompanied by tunable emission (Figure 5b). Moreover, the activated SPOC-SQ-a can selectively absorb acetylene (C_2H_2) over other gases without destroying the single crystallinity (Figure 5c), with a gate-opening sorption enthalpy of 33.0 kJ/mol (Figure 5d).

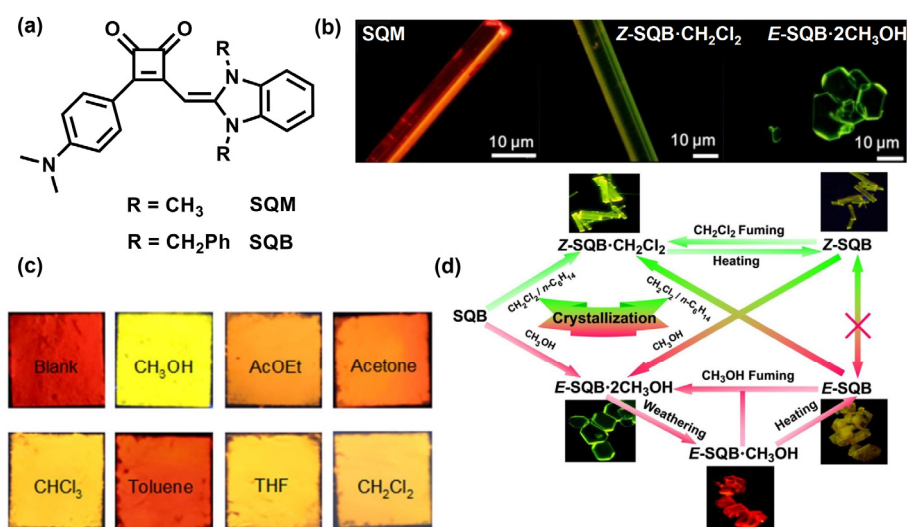


Figure 4. (a) Molecular structures of SQM and SQB. (b) Fluorescent images of crystal SQM, Z-SQB·CH₂Cl₂ and E-SQB·2CH₃OH taken by fluorescence microscopy. (c) The fluorescent images of E-SQB·CH₃OH after exposure to different solvent vapors under UV lamp illumination. (d) Schematic diagram of reversible thermochromism and vapochromism of the SQB·solvent assemblies. Adapted with permission from Ref. [36]. Copyright 2018, Wiley-VCH.

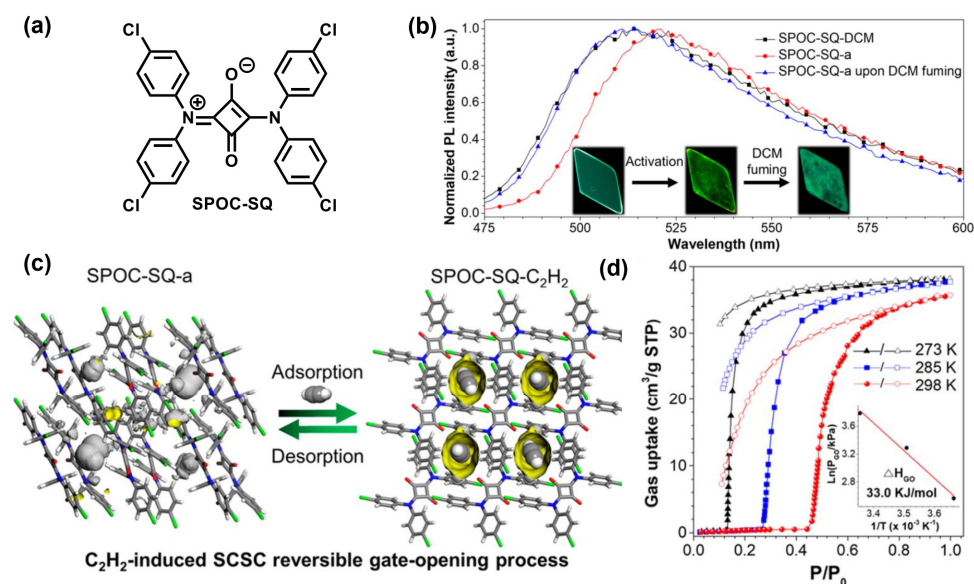


Figure 5. (a) Molecular structures of SPOC-SQ. (b) Fluorescent spectra of SPOC-SQ crystals including SPOC-SQ-DCM, SPOC-SQ-a, and SPOC-SQ-a after DCM fuming. Insets: fluorescent photographs of crystals taken by fluorescence microscopy. (c) C₂H₂-induced SCSC reversible gate-opening process. (d) Sorption isotherms of SPOC-SQ-a for C₂H₂ at different temperatures. Adapted with permission from Ref. [37]. Copyright 2021, American Chemical Society.

2.2. SQs with AIE Properties

Due to their out-of-order packing and strong dipole–dipole interaction, the AIE phenomenon is difficult to realize for SQ-based luminogens in aqueous solutions. To address this issue, we recently developed a new series of symmetrical and unsymmetrical SQs with AIE properties using tetraphenylethylene (TPE) functionalized diarylamine derivatives as the end groups [38]. The resulting TPE-SQ1-3 (Figure 6a) exhibited poor emission in solution state, but could emit intense emission in the nanoaggregated state in THF/H₂O mixtures (Figure 6b). The maximum emission peaks and emission efficiencies of pristine powders TPE-SQ1-3 were determined to be 548 nm ($\Phi_{\text{PLQY}} = 0.11$), 534 nm ($\Phi_{\text{PLQY}} = 0.13$),

and 695 nm ($\Phi_{\text{PLQY}} = 0.02$), respectively. Moreover, the symmetrical TPE-SQ1 and TPE-SQ2 powders also exhibited reversible mechanochromic characteristics with adjustable emission colors from yellow to orange red (Figure 6c,d), owing to the morphology change from the loose crystalline state to the tight amorphous state.

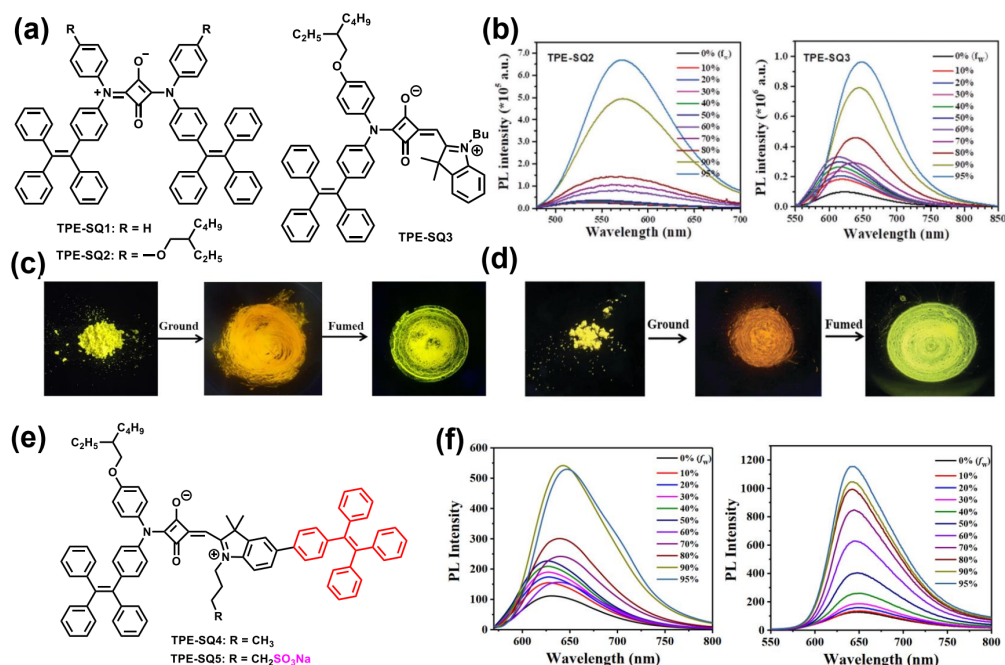


Figure 6. (a) Molecular structures of TPE-SQ1–3. (b) Fluorescent spectra of TPE-SQ2–3 in THF/H₂O mixtures with different water volume fractions. Mechanochromism fluorescence photographs of pristine, ground, and fumed TPE-SQ1 (c) and TPE-SQ2 (d) powders and under UV lamp illumination. Adapted with permission from Ref. [38]. Copyright 2020, Royal Society of Chemistry. (e) Molecular structures of TPE-SQ4 and TPE-SQ5. (f) Fluorescent spectra of TPE-SQ4 (left) in THF/H₂O mixtures with different water volume fractions and TPE-SQ5 (right) in THF/n-hexane mixtures with different n-hexane volume fractions. Reprinted with permission from Ref. [39]. Copyright 2021, Wiley-VCH.

To improve the emission efficiency of TPE-SQ3, we further synthesized two new unsymmetrical SQs by introducing an additional TPE unit on the indolenine end group, i.e., TPE-SQ4 and TPE-SQ5 (Figure 6e) [39]. The resulting TPE-SQ4 and TPE-SQ5 exhibited enhanced AIE properties and displayed intense, deep red emission in THF/H₂O mixtures when compared to TPE-SQ3 (Figure 6f). Interestingly, the solid-state Φ_{PLQY} of TPE-SQ4 was increased to 7.6%, while that of TPE-SQ5 was improved to 11% due to the introduction of an anionic sulfonate group (SO_3^-) that can enhance the molecular hydrophilicity and further modulate the intermolecular interactions.

Furthermore, we developed another SQ-based AIE luminogen (AIEgen) with deep-red emission based on pyrylium end group, namely TPE-SQ12 (Figure 7a) [40]. We found that the use of elastomer as the host polymer can significantly improve the thermoresponsive performance of AIEgens, and thus by doping a small amount of TPE-SQ12 into styrene-butadiene rubber (SBR), we obtained a high-performance, red-emissive, thermoresponsive film with high contrast ratio, fast response time (less than 3 s), and excellent reversible response (Figure 7b). Using this SBR/TPE-SQ12 film, double encryption for anti-counterfeiting and temperature mapping systems were successfully established (Figure 7c). Moreover, white emission was further realized by co-doping TPE-SQ12 with a cyan dye into SBR under UV irradiation (Figure 7d), delivering fluorescent thermochromism with enhanced temperature mapping ability.

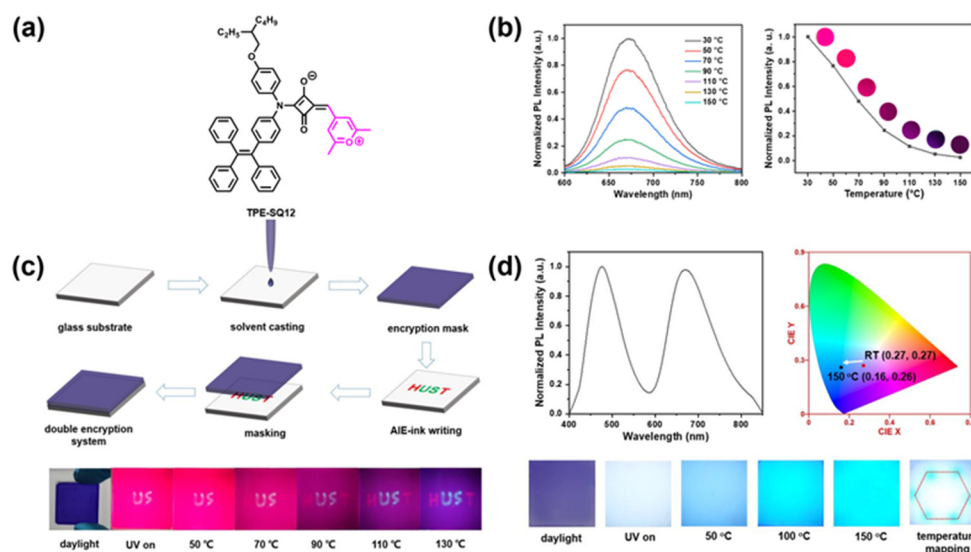


Figure 7. (a) Molecular structure of TPE-SQ12. (b) Temperature-dependent fluorescent spectra of SBR/TPE-SQ12 (left); fluorescent intensity versus temperature plots of SBR/TPE-SQ12 (right) (Inset: SBR/TPE-SQ12 films under UV lamp with different temperatures). (c) Double encryption system based on SBR/TPE-SQ12 film. Fabrication process (top). Photographs under daylight and UV lamp illumination at different temperatures (bottom). (d) Fluorescent spectra and CIE coordinates of TPE-SQ12/cyan dye co-doped SBR film (top). Photographs under daylight or under UV lamp illumination at different temperatures (bottom). Reprinted with permission from Ref. [40]. Copyright 2022, Wiley-VCH.

3. SQ-Based Functional Materials for Biomedical Applications

3.1. Fluorescent SQs as Biosensors

Selective and sensitive detection of a specific analyte is crucial when designing molecular probes. To date, SQs have been applied for sensing various specific analytes, such as metal ions, anions, nucleic acids, amino acid, proteins, and so on [7,28,41–43]. Different detection mechanisms have been developed, including metal coordination, nucleophilic addition, H-bond interaction, protonation/deprotonation, and aggregation/disaggregation, etc. [29] Here, based on these mechanisms, some representative works will be introduced.

In 2017, Lu et al. developed a “turn-on” far-red/NIR fluorescent sensor based on unsymmetrical SQ, i.e., SQ-DNBS (Figure 8a), for selective detection of thiophenol [44]. As depicted in Figure 8b,c, SQ-DNBS showed a colorimetric and “turn-on” fluorometric dual-channel transform for thiophenol in PBS solution, with high selectivity and sensitivity (detection limit: 9.9 nM). With the addition of thiophenol, the fluorescence of SQ-DNBS gradually increased at 645 nm with rapid response in PBS solution (Figure 8c), attributed to the cleavage reaction of SQ-DNBs mediated by thiophenol.

Pang et al. prepared a symmetrical SQ, namely SQ1 (Figure 8d), as a fluorescent sensor of glutathione (GSH) [45]. As illustrated in Figure 8e, due to strong aggregation of SQ1 in borate buffer solution, it showed very weak fluorescence. Upon addition of GSH to the SQ1 borate buffer solution, the fluorescence was notably enhanced at 630 and 820 nm in the presence of *o*-phthalaldehyde (OPA, react with GSH formation of isoindole-GSH derivative at room temperature). Owing to a strong interaction between isoindole-GSH and SQ1, the SQ1 disaggregated and self-assembled with isoindole-GSH (Figure 8f).

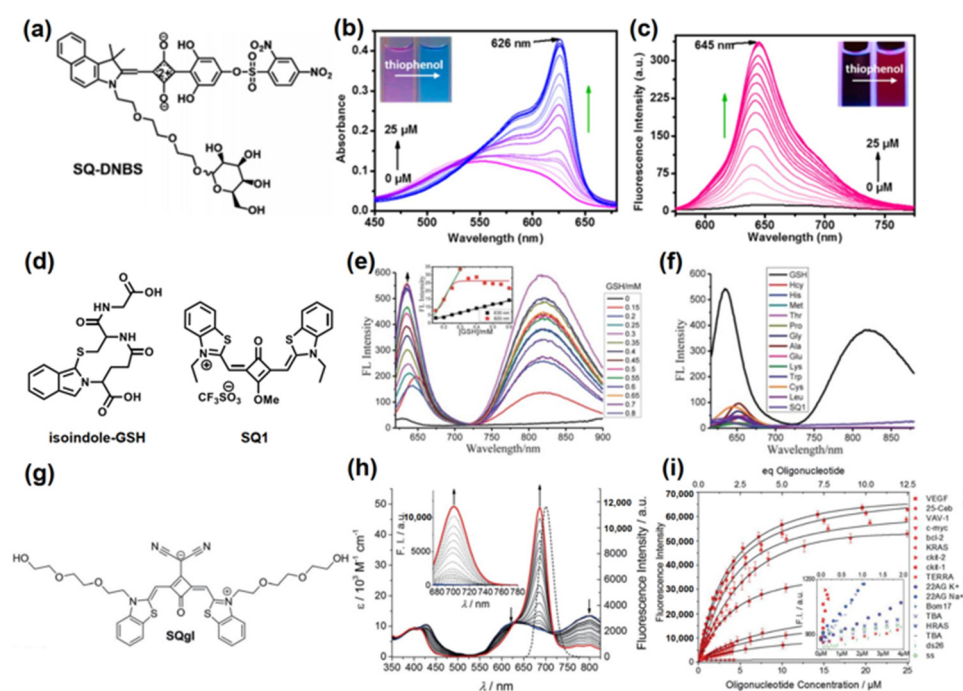


Figure 8. (a) Molecular structure of SQ-DNBS. (b) Absorption spectra of SQ-DNBS with the addition of different concentrations of thiophenol in PBS. (c) Fluorescent spectra of SQ-DNBS with the addition of different concentrations of thiophenol in PBS. Reprinted with permission from Ref. [44]. Copyright 2017, American Chemical Society. (d) Molecular structures of SQ1 and isoindole-GSH. (e) Fluorescent spectra of SQ1 with the addition of different concentrations of GSH in borate buffer. (f) Fluorescent spectra of SQ1 in the presence of OPA, 11 different kinds of amino acids and Hcy. Adapted with permission from Ref. [45]. Copyright 2013, Royal Society of Chemistry. (g) Molecular structure of SQgl. (h) Absorption (solid lines) and fluorescent (dotted lines, inset) spectra of SQgl with the addition of different concentrations of VAV-1 in buffer solution. (i) Fluorescent titrations curves of SQgl buffered solution with the oligonucleotides showing in the legend. Adapted with permission from Ref. [46]. Copyright 2017, Wiley-VCH.

Würthner et al. reported a new amphiphilic core-substituted SQgl (Figure 8g) as an NIR “turn-on” fluorescent probe to detect VAV-1 (G4s, one of the G-quadruplexes, which are DNA or RNA tertiary structures) with high selectivity [46]. As shown in Figure 8h, SQgl formed a nonfluorescent aggregate by self-assembly in buffer solution. However, upon addition of VAV-1, the fluorescent intensity at 700 nm was pronouncedly enhanced by forming a sandwich-like SQgl/G4 1:2 complex, accompanied by significantly increased Φ_{PLQY} up to 0.61 in the far-red/NIR region.

As discussed in above, our group has developed a series of SQ-based deep-red-emissive AIEgens, i.e., TPE-SQ3-5 (Figure 6) [39]. We further encouragingly found that they could serve as high performance ClO^- sensors with high selectivity and sensitivity (Figure 9a–e). The results showed that TPE-SQ3 and TPE-SQ4 are “turn-off” fluorescent probes (Figure 9b), while TPE-SQ5 is a ratiometric fluorescent probe (detection limit: 5.6 nM) (Figure 9d). The sensing mechanism indicated that when detecting ClO^- , an oxindole product is generated for TPE-SQ5 (the key for ratiometric fluorescence), while an epoxide product is obtained for TPE-SQ4. In addition, TPE-SQ5 can be fabricated into nanoparticles (NPs) with biocompatible nonionic Pluronic F-127. The resulting TPE-SQ5 NPs exhibited excellent biocompatibility and low cytotoxicity, and can sensitively image exogenous and endogenous ClO^- in living cells (Figure 9f).

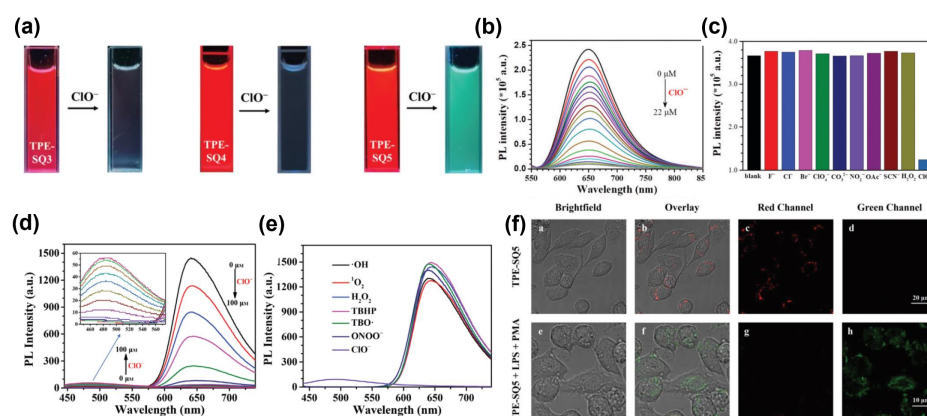


Figure 9. (a) The fluorescent photographs of TPE-SQ3-5 before and after adding ClO^- (10 equivalent) in 95% $\text{H}_2\text{O}/\text{THF}$ mixtures under UV lamp irradiation. (b) The fluorescent spectra of TPE-SQ3 with the addition of different concentrations of ClO^- . (c) Histogram of the fluorescent spectra of TPE-SQ3 in the presence of ClO^- and different anions. Reprinted with permission from Ref. [38]. Copyright 2020, Royal Society of Chemistry. (d) The fluorescent spectra of TPE-SQ5 in the presence of different concentrations of ClO^- . (e) The fluorescent spectra of TPE-SQ5 in the presence of ClO^- and different ROSs. (f) The fluorescent images incubated with TPE-SQ5 NPs for ClO^- detection in living RAW264.7 cells using confocal microscopy. Adapted with permission from Ref. [39]. Copyright 2021, Wiley-VCH.

3.2. Fluorescent SQs for Bioimaging

Due to their intense deep-red and NIR emission, high photostability and low cytotoxicity, SQs have also been investigated for *in vitro* and *in vivo* bioimaging [47–49]. Currently there are two different methods for SQs to realize effective bioimaging: direct conjugation with a targeting ligand and nano-precipitation [21]. For example, we demonstrated that TPE-SQ3-based NPs encapsulated by amphiphilic polymer PEG-*b*-PCL can bring bright far-red cell fluorescence with outstanding photostability when used for 4T1 cell imaging [38].

Xi et al. reported a new core-substituted SQ, i.e., MitoESq-635, by specifically connecting SQ to the membrane proteins in the mitochondria, as shown in Figure 10a [50]. By adopting super-resolution technology, MitoESq-635 was investigated as a bioimaging reagent to image the dynamic structures of mitochondrial cristae in living HeLa cells. As shown in Figure 10b,c, the stimulated emission depletion (STED) imaging of the living HeLa cells incubated with MitoESq-635 showed low saturation intensity and high photostability. Meanwhile, the time-lapse imaging of the mitochondrial inner membrane in living HeLa cells was carried out with an outstanding resolution of 35.2 nm.

Zhao et al. developed a NIR-absorbing quinoline-based SQ for *in vivo* fluorescence and photoacoustic imaging, namely D1 (Figure 10d) [51]. Dicyanomethylene substitution at the center of squarate bridge results in redshifted absorption and emission, and increased Φ_{PLQY} . D1 was encapsulated with the biocompatible Pluronic F-127 to obtain NPs ($\text{D1}_{\text{micelle}}$) in aqueous conditions with low cytotoxicity. The resulting $\text{D1}_{\text{micelle}}$ not only showed high fluorescent intensity in Huh-7 cells (Figure 10e), but also emitted strong NIR fluorescence signal in thoracic/abdominal area of the mouse (Figure 10f). Besides, the photoacoustic imaging capability of $\text{D1}_{\text{micelle}}$ was also studied, and a high signal intensity was observed at 840 nm (Figure 10g), showing favorable photoacoustic imaging ability.

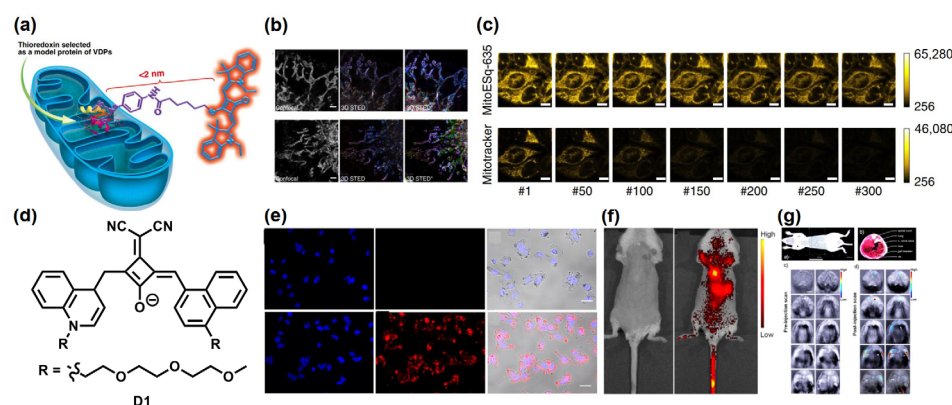


Figure 10. (a) Molecular structure and schematic diagram of MitoESq-635 for mitochondrial dynamics imaging. (b) Color-coded STED imaging of the 3D stack in cancer cells. (c) The fluorescence intensity curves and imaging of HeLa cells incubated with MitoESq-635 (top) and MitoTracker Green (bottom). Reprinted with permission from Ref. [50]. Copyright 2020, Nature Publishing Group. (d) Molecular structure of D1. (e) Fluorescent images of the Huh-7 cells incubated with D1 (top) and D1_{micelle} (bottom) by confocal microscopy. (f) Fluorescent images of a mouse were measured before (left) and after (right) of intravenous injection with D1_{micelle}. (g) The photoacoustic images of a live mouse anatomy. Adapted with permission from Ref. [51]. Copyright 2015, American Chemical Society.

In addition to the core-substituted SQs described above, symmetrical and unsymmetrical SQs have also been successfully explored as the bioimaging materials. Delcamp et al. recently synthesized a water-soluble NIR-absorbing SQ, namely SO₃SQ (Figure 11a), using the indolizine derivatives as end groups [52]. SO₃SQ showed a very high Φ_{PLQY} of 58% with absorption and emission >700 nm in fetal bovine serum (Figure 11b). Compared to FDA approved dye indocyanine green (ICG), SO₃SQ exhibited higher molecular brightness and prolonged photostability, making it an attractive potential NIR biological imaging material with low cytotoxicity (Figure 11c).

Recently, Choi et al. also developed a series of unsymmetrical SQ, i.e., OCTL12-16 (Figure 11d) [53]. The surface charges of SQs are suitable for rapid transporter-mediated cellular uptake. As shown in Figure 11e, OCTL14 showed excellent lysosome-targeting ability (76.2%), optimal optical and pharmacokinetic profiles due to the positive charge of the quaternary anion. Dual fluorescence imaging of tumors and ureters incubated with OCTL14 and ZW800-PEG showed high specificity and sensitivity after a single intravenous injection (Figure 11f).

Additionally, SQ-based conjugated polymers were also developed in bioimaging. Compared to the small molecules, they showed larger Stokes shifts and higher Φ_{PLQY} s in the NIR region [54]. For example, Chiu et al. developed a series of SQ-based, pH-responsive NIR emitters with high photostability, i.e., PFSqG0-2 (Figure 12a), by covalently incorporating SQs into the polyfluorene backbone [55]. When the concentration of SQ backbone was less than 5%, the fluorescence self-quenching of these SQ-based polymers was effectively suppressed. As shown in Figure 12b, PFSqG2-5% can be used to detect the tiny intracellular pH changes effectively in living MCF7 cells.

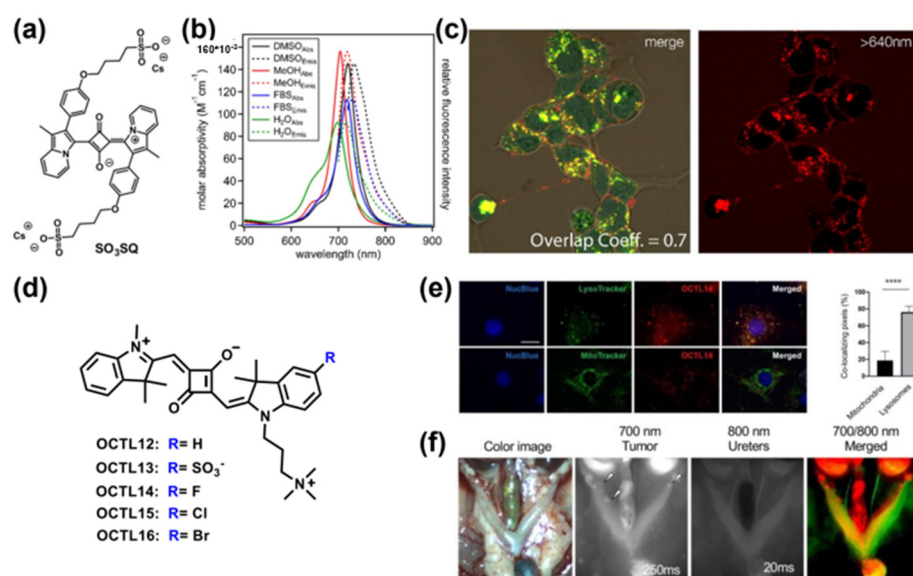


Figure 11. (a) Molecular structure of SO₃SQ. (b) The molar absorptivity and normalized fluorescence emission of SO₃SQ in Vis-NIR region. (c) The confocal images of living S2 cells incubated with SO₃SQ and LysoTracker. Reprinted with permission from Ref. [52]. Copyright 2020, American Chemical Society. (d) Molecular structures of OCTL12-16. (e) Subcellular localization (left) of ID8 cells incubated with OCTL14 for 30 min. Co-localization index (right) of OCTL14 with LysoTracker Red or MitoTracker Green. **** $p < 0.0001$ by two-tailed Student's *t*-test. (f) Dual fluorescent imaging of tumors and ureters incubated with OCTL14 and ZW800-PEG, respectively. Adapted with permission from Ref. [53]. Copyright 2022, Wiley-VCH.

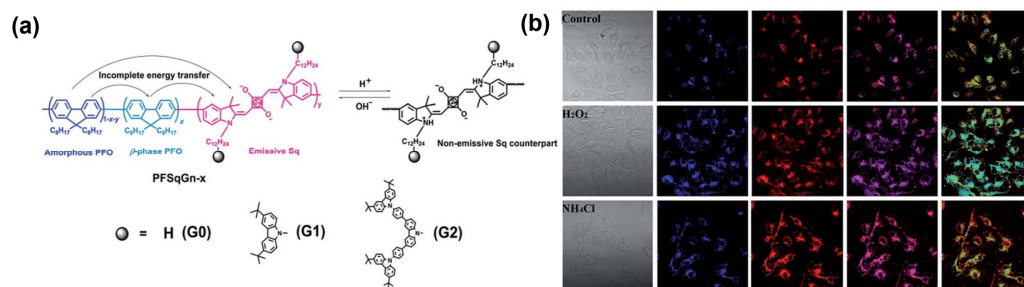


Figure 12. (a) Molecular structures of PFSqG0-2 polymers. (b) The fluorescent images of MCF-7 cells incubated with PFSqG2—5% and treated with NH₄Cl and H₂O₂ in pH 7.4 PBS buffer solution using confocal microscopy upon laser illumination. Reprinted with permission from Ref. [55]. Copyright 2017, Royal Society of Chemistry.

Up-conversion luminescence (UCL) is a special process whereby long wavelength photons are converted into shorter wavelength photons by efficient energy-transfer processes [56]. In two-photon absorption (TPA), one molecule absorbs two photons simultaneously when excited, and the two-photon fluorescence belongs to UCL, which shows good spatial selectivity and less damage to samples compared with those of the one-photon process [57]. SQs with high TPA cross-section (δ) value were successfully designed, including extended π -systems and various conjugated D/A units [58]. Zhang et al. reported a series of symmetrical SQs for TPA bioimaging, i.e., ISD-1-7 (Figure 13a) [59]. Among the series, ISD-7 had a remarkable TPA δ value above 8000 GM at 780 nm (Figure 13b), which is suitable for the optical window in biological tissue. Hence, ISD-7 was successfully employed in NIR fibroblast cell imaging and in vivo cerebrovascular blood fluid tracing (Figure 13c) using two-photon laser confocal scanning microscopy. Recently, Belfield and Hagan et al. also developed an unsymmetrical SQ with charged nonconjugated substituent [60], offering bright red fluorescence two-photon imaging of HeLa cells.

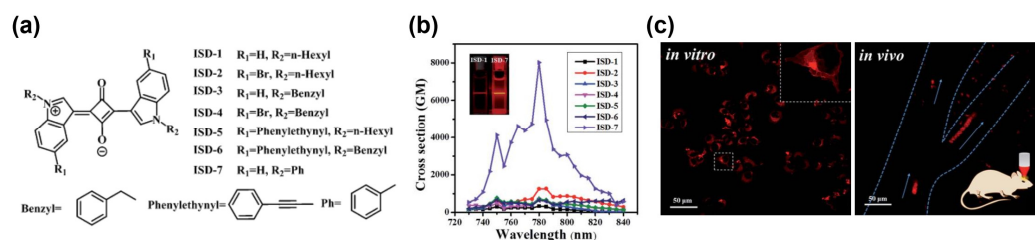


Figure 13. (a) Molecular structures of ISD compounds. (b) Two-photon absorption (TPA) cross-section curves of ISDs in THF solutions. Inset: TPA fluorescence photographs of ISD-1 (left) and the ISD-7 (right) in solution under laser illumination. (c) Confocal scanning microscopy images of fibroblast cells (left) and the blood plasma in blood vessels (right) incubated with ISD-7 upon two-photon laser illumination. Adapted with permission from Ref. [59]. Copyright 2015, Royal Society of Chemistry.

3.3. Fluorescent SQs for PTT and PDT

Wang et al. developed a dicyanomethylene-substituted SQ (Figure 14a) with high photostability [61]. Biocompatible supramolecular adduct SQ₂BSA was achieved by hydrophobic and H-bonding interactions between SQ and bovine serum albumin (BSA), leading to 80-fold fluorescence enhancement. Meanwhile, to enhance the targeting ability of SQ₂BSA, folic acid (FA) was chosen as the targeting ligand to conjugate to SQ₂BSA. The resulting SQ₂BSA-FA was cultivated in KB cells, and most of these were dead treated with NIR laser (Figure 14b), resulting in a notable PTT effect. Subsequently, photothermal tumor therapy studies *in vivo* were carried out in KB cells xenografted nude mouse models, demonstrating SQ₂BSA-FA as one of the potential photothermal materials for antitumor therapy under NIR window (Figure 14c).

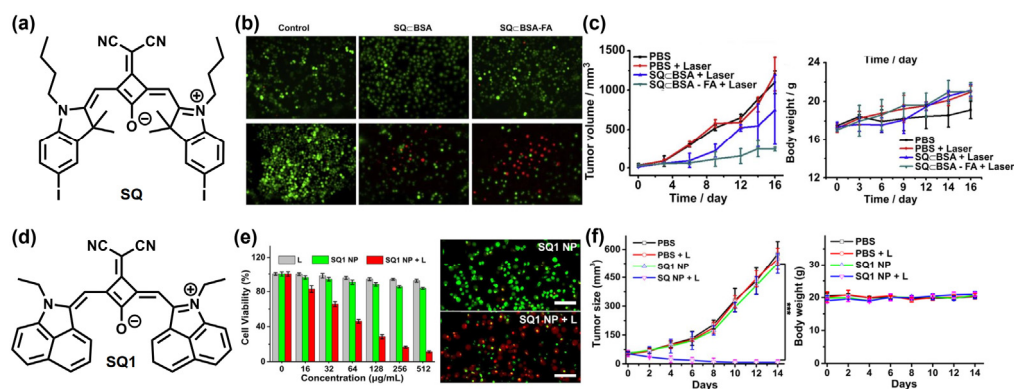


Figure 14. (a) Molecular structure of SQ. (b) Live/dead cell staining assays of KB cells incubated with control, SQ₂BSA and SQ₂BSA-FA treated with (top) and without (bottom) NIR laser. (c) The tumor volume curves (left) and body weight change curves (right) of mice bearing KB tumors with PBS, PBS + Laser, SQ₂BSA + Laser and SQ₂BSA-FA + Laser. Reprinted with permission from Ref. [61]. Copyright 2014, Elsevier Ltd. (d) Molecular structure of SQ1. (e) Cell viability (left) and live/dead cell staining assays (right) of breast cancer cells after treatment with different concentrations of SQ1 NP with or without NIR laser irradiation. (f) Tumor growth curves (left) and body weight (right) treated with PBS, PBS + laser, SQ1 NP and SQ1 NP + laser. Adapted with permission from Ref. [62]. Copyright 2020, American Chemical Society.

Recently, Wang et al. reported a new SQ (SQ1, Figure 14d) employing the same core but with 1,8-naphtholactam as the end group [62]. SQ1 was encapsulated with the amphiphilic polymer DSPE-PEG and the peptide CREKA to obtain NPs (SQ1 nanoprobe), showing excellent NIR-II fluorescence imaging and photoacoustic imaging. Figure 14e shows that SQ1 NPs can kill most MDA-MB-231 cells under NIR irradiation as a result of efficient photothermal effects, while most cells were alive in the control group. In addition, MDAMB-231 breast cancer tumor-bearing mice were used to study the photothermal

therapeutic efficiency, indicating that the tumor growth of the SQ1 nanoprobe-treated group upon NIR irradiation was effectively suppressed when compared to other control groups (Figure 14f).

Dicyanomethylene-substituted SQ also showed good performance in PDT. Shang-guan et al. developed a series of SQs, i.e., CSBE, CSME, CSBM, and CSTS (Figure 15a), with benzothiazole derivatives as the end groups [63]. These molecules showed negligible dark toxicity in multiple cancer cells tested by CCK-8 assay. However, under laser irradiation, they could generate singlet oxygen as photosensitizers, thereby efficiently killing the cancer cells (Figure 15b). Among them, CSBE showed the strongest photo-cytotoxicity under laser irradiation at 690 nm. In addition, CSBE was injected into tumor-bearing mice for further PDT, and the pathological features of tumors of CSBE + light group showed severe cellular damage, leading to significantly decreased tumor volume compared to the control groups (Figure 15c).

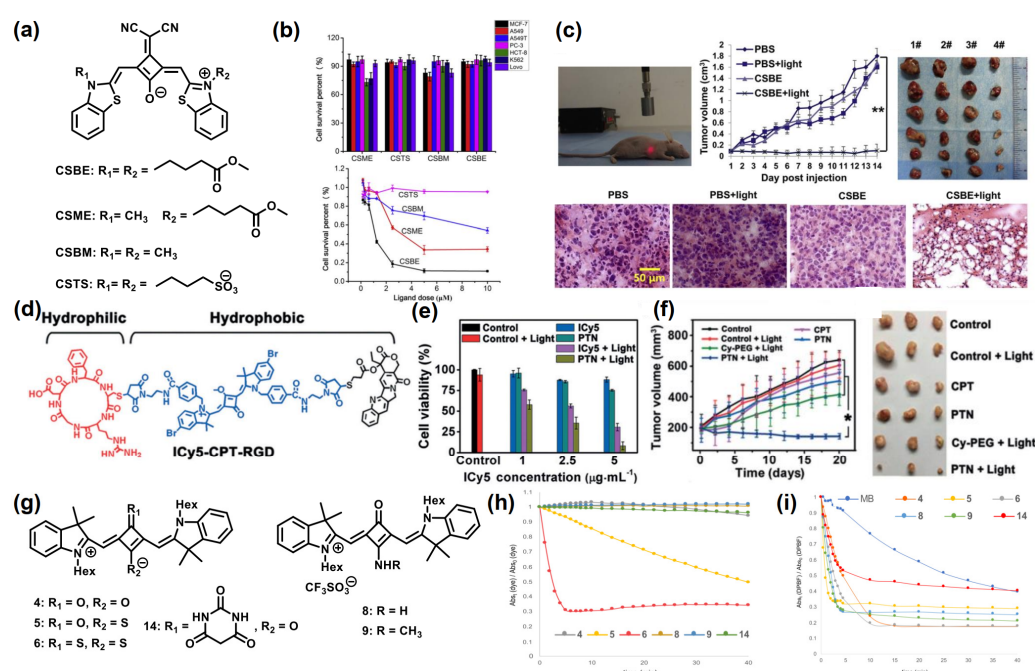


Figure 15. (a) Molecular structures of CSBE, CSME, CSBM, and CSTS. (b) Cell viability of different cancer cells after treatment with CSBE, CSME, CSBM, and CSTS (top). Viability of MCF-7 cells treated with different concentrations of CSBE, CSME, CSBM, and CSTS under laser irradiation (bottom). (c) The corresponding PDT results treated with CSBE. Reprinted with permission from Ref. [63]. Copyright 2017, Elsevier Ltd. (d) Molecular structure of ICy5-CPT-RGD. (e) Cell viability of BEL-7402 cells treated with control group, ICy5, and PNT, with or without laser irradiation. (f) Tumor growth curves (left) and photographs of tumors (right) of tumor-bearing mice treated with PBS (control), control + light, CPT, PTN, Cy-PEG + light, and PTN + light. Reprinted with permission from Ref. [64]. Copyright 2018, Wiley-VCH. (g) Molecular structures of SQs 4–6, 8, 9 and 14 with different groups. (h) Photostability experiment of SQs 4–6, 8, 9 and 14 in DMSO. (i) Qualitative $^1\text{O}_2$ generation ability test of SQs 4–6, 8, 9, 14 and MB in PBS solution. Adapted with permission from Ref. [65]. Copyright 2019, Elsevier Ltd.

Yin et al. reported a new SQ-based molecule (ICy5) with aggregation-enhanced photodynamic efficiency (Figure 15d) [64]. By covalently attaching amphiphilic groups to functionalize ICy5, the self-assembled phototheranostic nanodrug (PTN) was obtained in water with high $^1\text{O}_2$ production ability. The CCK-8 assay showed that ICy5 had low dark toxicity in both normal cells and cancer cells under the dark, while PTN caused the death of most human hepatoma (BEL-7402) cells after light irradiation, indicating significant cytotoxicity to cancer cells (Figure 15e). The fluorescent imaging of PTN demonstrated its

excellent tumor-targeting ability in vivo (Figure 15f). Moreover, BEL-7402 tumor-bearing mice were investigated to evaluate the tumor-inhibition efficiency of PTN in vivo, which indicated that the mice treated with PTN exhibited excellent tumor-inhibition efficiency under light irradiation.

Recently, Reis and Silvestre et al. further synthesized a series of SQs with different groups on the central oxygen atoms, such as sulfur, barbituric acid, amino, and methylamino (Figure 15g) [65]. Excluding monothio- and dithio-SQs, these SQs presented good photostability (Figure 15h). Besides, in vitro potential of these SQs as photosensitizers for PDT was evaluated in several tumor and non-tumor cell lines, and the results indicated that all of SQs have effective $^1\text{O}_2$ generation capacity under a custom-built LED irradiation compared with FDA approved dye methylene blue (MB) (Figure 15i).

4. Conclusions

In this review, representative SQ-based fluorescent materials and their applications for biosensing, bioimaging and phototherapy have been summarized, as shown in Table 1, and the current research results have strongly suggested that SQs are attractive material candidates for biomedics. However, there are still some challenges to be resolved. First of all, most SQs suffer from severe aggregation, leading to quenched fluorescence and reduced PDT efficiency in their aggregation state. Endowing SQs with AIE property is a feasible solution, however, efficient structural design strategies are still lacking. Moreover, further efforts are needed to improve the targeting ability and phototherapy effect of SQs. On the other hand, NIR absorption/emission beyond 950 nm is highly necessary for bioimaging, due to the requirement of matching the optical transparency window of biological tissues. However, it remains a significant challenge to extend the absorption/emission to this wavelength region, due to the fixed conjugation length of SQs. In this context, controlling the aggregation behaviors in a favorable manner, such as achieving supramolecular J-aggregates, will be an attractive approach.

Table 1. A summary of representative SQs for biomedical applications.

Categories	Compounds	Absorbance λ_{max} (nm)	Emission λ_{max} (nm)	Biomedical Applications	References
symmetrical	SO3SQ	720 ¹	734 ¹	Cell imaging	[52]
	ISD-1	560 ²	580 ²	Cells and mice imaging	[59]
	ISD-2	561 ²	581 ²	Cells and mice imaging	[59]
	ISD-3	562 ²	582 ²	Cells and mice imaging	[59]
	ISD-4	561 ²	582 ²	Cells and mice imaging	[59]
	ISD-5	561 ²	582 ²	Cells and mice imaging	[59]
	ISD-6	578 ²	598 ²	Cells and mice imaging	[59]
	ISD-7	575 ²	600 ²	Cells and mice imaging	[59]
	4	645 ¹	-	Cell imaging	[65]
unsymmetrical	TPE-SQ3	547 ³	625 ³	Detect ClO^- , Cell imaging	[38]
	TPE-SQ4	561 ³	629 ³	Detect ClO^- , Cell imaging	[39]
	TPE-SQ5	536 ³	652 ³	Detect ClO^- , Cell imaging	[39]
	SQ-DNBS	553 ⁴	-	Detect thiophenol	[44]
	OCTL12	635 ⁴	652 ⁴	Cells and mice imaging	[53]
	OCTL13	636 ⁴	650 ⁴	Cells and mice imaging	[53]
	OCTL14	635 ⁴	649 ⁴	Cells and mice imaging	[53]
	OCTL15	637 ⁴	650 ⁴	Cells and mice imaging	[53]
	OCTL16	637 ⁴	657 ⁴	Cells and mice imaging	[53]
	ICy5-CPT-RGD	654 ⁵	665 ⁵	PDT	[64]

Table 1. Cont.

Categories	Compounds	Absorbance λ_{\max} (nm)	Emission λ_{\max} (nm)	Biomedical Applications	References
core-substituted	SQ1	530 ⁶	630 ⁶	Detect GSH	[45]
	SQgl	708 ³	744 ³	Detect VAV-1	[46]
	MitoESq-635	635 ¹	670 ¹	Cell imaging	[50]
	D1	867 ¹	907 ¹	Cells and mice imaging	[51]
	SQ	705 ³	718 ³	PTT	[61]
	SQ1	930 ³	970 ³	PTT	[62]
	CSBE	~600 ⁴	-	PDT	[63]
	CSME	~600 ⁴	-	PDT	[63]
	CSBM	~600 ⁴	-	PDT	[63]
	CSTS	~600 ⁴	-	PDT	[63]
	5	649 ¹	-	PDT	[65]
	6	663 ¹	-	PDT	[65]
	8	651 ¹	-	PDT	[65]
	9	662 ¹	-	PDT	[65]
14	658 ¹	-	PDT	[65]	

¹ In DMSO. ² Not mentioned. ³ In THF. ⁴ In PBS. ⁵ In FBS. ⁶ In borate buffer solution.

Author Contributions: Conceptualization, Z.L. and W.Q.; writing—original draft preparation, W.Q.; writing—review and editing, Z.L.; supervision, Z.L.; funding acquisition, Z.L. All authors have read and agreed to the published version of the manuscript.

Funding: This research was funded by the Natural Science Foundation of China (No. 22175067; 21975085) and Excellent Youth Foundation of Hubei Scientific Committee (2021CFA065).

Institutional Review Board Statement: Not applicable.

Informed Consent Statement: Not applicable.

Data Availability Statement: Not applicable.

Acknowledgments: The authors would also like to thank the Analytical and Testing Center at HUST for the use of their facilities.

Conflicts of Interest: The authors declare no conflict of interest.

References

- Wu, D.; Chen, L.; Lee, W.; Ko, G.; Yin, J.; Yoon, J. Recent progress in the development of organic dye based near-infrared fluorescence probes for metal ions. *Coord. Chem. Rev.* **2018**, *354*, 74–97. [CrossRef]
- Yuan, L.; Lin, W.; Zheng, K.; He, L.; Huang, W. Far-red to near infrared analyte-responsive fluorescent probes based on organic fluorophore platforms for fluorescence imaging. *Chem. Soc. Rev.* **2013**, *42*, 622–661. [CrossRef] [PubMed]
- Cai, Y.; Si, W.; Huang, W.; Chen, P.; Shao, J.; Dong, X. Organic Dye Based Nanoparticles for Cancer Phototheranostics. *Small* **2018**, *14*, 1704247. [CrossRef] [PubMed]
- Gsänger, M.; Bialas, D.; Huang, L.; Stolte, M.; Würthner, F. Organic Semiconductors based on Dyes and Color Pigments. *Adv. Mater.* **2016**, *28*, 3615–3645. [CrossRef] [PubMed]
- Würthner, F.; Kaiser, T.E.; Saha-Möller, C.R. J-Aggregates: From Serendipitous Discovery to Supramolecular Engineering of Functional Dye Materials. *Angew. Chem. Int. Ed.* **2011**, *50*, 3376–3410. [CrossRef]
- Chan, J.; Dodani, S.C.; Chang, C.J. Reaction-based small-molecule fluorescent probes for chemoselective bioimaging. *Nat. Chem.* **2012**, *4*, 973–984. [CrossRef]
- Sun, W.; Guo, S.; Hu, C.; Fan, J.; Peng, X. Recent Development of Chemosensors Based on Cyanine Platforms. *Chem. Rev.* **2016**, *116*, 7768–7817. [CrossRef]
- Li, Y.; Zhou, Y.; Yue, X.; Dai, Z. Cyanine conjugates in cancer theranostics. *Bioact. Mater.* **2021**, *6*, 794–809. [CrossRef]
- Sreejith, S.; Carol, P.; Chithra, P.; Ajayaghosh, A. Squaraine dyes: A mine of molecular materials. *J. Mater. Chem.* **2008**, *18*, 264–274. [CrossRef]
- Khopkar, S.; Shankarling, G. Synthesis, photophysical properties and applications of NIR absorbing unsymmetrical squaraines: A review. *Dyes Pigment.* **2019**, *170*, 107645. [CrossRef]
- Beverina, L.; Salice, P. Squaraine Compounds: Tailored Design and Synthesis towards a Variety of Material Science Applications. *Eur. J. Org. Chem.* **2010**, *2010*, 1207–1225. [CrossRef]

12. Maltese, V.; Cospito, S.; Beneduci, A.; De Simone, B.C.; Russo, N.; Chidichimo, G.; Janssen, R.A.J. Electro-optical Properties of Neutral and Radical Ion Thienosquaraines. *Chem. Eur. J.* **2016**, *22*, 10179–10186. [[CrossRef](#)] [[PubMed](#)]
13. Corrente, G.A.; Parisi, F.; Maltese, V.; Cospito, S.; Imbardelli, D.; La Deda, M.; Beneduci, A. Panchromatic Fluorescence Emission from Thienosquaraines Dyes: White Light Electrofluorochromic Devices. *Molecules* **2021**, *26*, 6818. [[CrossRef](#)] [[PubMed](#)]
14. Chen, G.; Sasabe, H.; Igarashi, T.; Hong, Z.; Kido, J. Squaraine dyes for organic photovoltaic cells. *J. Mater. Chem. A* **2015**, *3*, 14517–14534. [[CrossRef](#)]
15. Xiao, Q.; Tian, J.; Xue, Q.; Wang, J.; Xiong, B.; Han, M.; Li, Z.; Zhu, Z.; Yip, H.-L.; Li, Z.A. Dopant-Free Squaraine-Based Polymeric Hole-Transporting Materials with Comprehensive Passivation Effects for Efficient All-Inorganic Perovskite Solar Cells. *Angew. Chem. Int. Ed.* **2019**, *58*, 17724–17730. [[CrossRef](#)]
16. Treibs, A.; Jacob, K. Cyclotrimethine Dyes Derived from Squaric Acid. *Angew. Chem. Int. Ed.* **1965**, *4*, 694. [[CrossRef](#)]
17. Saccone, D.; Galliano, S.; Barbero, N.; Quagliotto, P.; Viscardi, G.; Barolo, C. Polymethine Dyes in Hybrid Photovoltaics: Structure–Properties Relationships. *Eur. J. Org. Chem.* **2016**, *2016*, 2244–2259. [[CrossRef](#)]
18. Shi, Q.; Chen, W.-Q.; Xiang, J.; Duan, X.-M.; Zhan, X. A Low-Bandgap Conjugated Polymer Based on Squaraine with Strong Two-Photon Absorption. *Macromolecules* **2011**, *44*, 3759–3765. [[CrossRef](#)]
19. Xiao, Q.; Wu, F.; Han, M.; Li, Z.; Zhu, L.; Li, Z. A pseudo-two-dimensional conjugated polysquaraine: An efficient p-type polymer semiconductor for organic photovoltaics and perovskite solar cells. *J. Mater. Chem. A* **2018**, *6*, 13644–13651. [[CrossRef](#)]
20. He, J.; Jo, Y.J.; Sun, X.; Qiao, W.; Ok, J.; Kim, T.; Li, Z.A. Squaraine Dyes for Photovoltaic and Biomedical Applications. *Adv. Funct. Mater.* **2021**, *31*, 2008201. [[CrossRef](#)]
21. Xiao, Q.; Li, Y.; Han, M.; Wu, F.; Leng, X.; Zhang, D.; Zhang, X.; Yang, S.; Zhang, Y.; Li, Z.A.; et al. Rational Design of 2D p– π Conjugated Polysquaraines for Both Fullerene and Nonfullerene Polymer Solar Cells. *Macromol. Chem. Phys.* **2020**, *221*, 1900439. [[CrossRef](#)]
22. Ilina, K.; MacCuaig, W.M.; Laramie, M.; Jeouty, J.N.; McNally, L.R.; Henary, M. Squaraine Dyes: Molecular Design for Different Applications and Remaining Challenges. *Bioconjug. Chem.* **2020**, *31*, 194–213. [[CrossRef](#)] [[PubMed](#)]
23. Ronchi, E.; Ruffo, R.; Rizzato, S.; Albinati, A.; Beverina, L.; Pagani, G.A. Regioselective Synthesis of 1,2- vs 1,3-Squaraines. *Org. Lett.* **2011**, *13*, 3166–3169. [[CrossRef](#)] [[PubMed](#)]
24. Mayerhöffer, U.; Gsänger, M.; Stolte, M.; Fimmel, B.; Würthner, F. Synthesis and Molecular Properties of Acceptor-Substituted Squaraine Dyes. *Chem. Eur. J.* **2013**, *19*, 218–232. [[CrossRef](#)] [[PubMed](#)]
25. Wu, J.; Yang, D.; Wang, Q.; Yang, L.; Sasabe, H.; Sano, T.; Kido, J.; Lu, Z.; Huang, Y. Central dicyanomethylene-substituted unsymmetrical squaraines and their application in organic solar cells. *J. Mater. Chem. A* **2018**, *6*, 5797–5806. [[CrossRef](#)]
26. Khopkar, S.; Deshpande, S.; Shankarling, G. Greener Protocol for the Synthesis of NIR Fluorescent Indolenine-Based Symmetrical Squaraine Colorants. *ACS Sustain. Chem. Eng.* **2018**, *6*, 10798–10805. [[CrossRef](#)]
27. Zappimulso, N.; Capozzi, M.A.M.; Porcheddu, A.; Farinola, G.M.; Punzi, A. Solvent-free Reactions for the Synthesis of Indolenine-based Squaraines and Croconaines: Comparison of Thermal Heating, Mechanochemical Milling, and IR Irradiation. *ChemSusChem* **2021**, *14*, 1363–1369. [[CrossRef](#)]
28. Ta, D.D.; Dzyuba, S.V. Squaraine-Based Optical Sensors: Designer Toolbox for Exploring Ionic and Molecular Recognitions. *Chemosensors* **2021**, *9*, 302. [[CrossRef](#)]
29. Xia, G.; Wang, H. Squaraine dyes: The hierarchical synthesis and its application in optical detection. *J. Photochem. Photobiol. C Photochem. Rev.* **2017**, *31*, 84–113. [[CrossRef](#)]
30. Feng, G.; Zhang, G.Q.; Ding, D. Design of superior phototheranostic agents guided by Jablonski diagrams. *Chem. Soc. Rev.* **2020**, *49*, 8179–8234. [[CrossRef](#)]
31. Wu, W.; Li, Z. Nanoprobes with aggregation-induced emission for theranostics. *Mater. Chem. Front.* **2021**, *5*, 603–626. [[CrossRef](#)]
32. Yoshii, R.; Hirose, A.; Tanaka, K.; Chujo, Y. Functionalization of Boron Diiminates with Unique Optical Properties: Multicolor Tuning of Crystallization-Induced Emission and Introduction into the Main Chain of Conjugated Polymers. *J. Am. Chem. Soc.* **2014**, *136*, 18131–18139. [[CrossRef](#)] [[PubMed](#)]
33. Luo, J.; Xie, Z.; Lam, J.W.Y.; Cheng, L.; Chen, H.; Qiu, C.; Kwok, H.S.; Zhan, X.; Liu, Y.; Zhu, D.; et al. Aggregation-induced emission of 1-methyl-1,2,3,4,5-pentaphenylsilole. *Chem. Commun.* **2001**, *18*, 1740–1741. [[CrossRef](#)] [[PubMed](#)]
34. Yang, S.; You, J.; Lan, J.; Gao, G. Facile Access to Extremely Efficient Energy-Transfer Pairs via an Unexpected Reaction of Squaraines with Ketones. *J. Am. Chem. Soc.* **2012**, *134*, 11868–11871. [[CrossRef](#)]
35. Yang, S.; Yin, P.-A.; Li, L.; Peng, Q.; Gu, X.; Gao, G.; You, J.; Tang, B.Z. Crystallization-Induced Reversal from Dark to Bright Excited States for Construction of Solid-Emission-Tunable Squaraines. *Angew. Chem. Int. Ed.* **2020**, *59*, 10136–10142. [[CrossRef](#)]
36. Xia, G.; Shen, S.; Hu, X.-M.; Jiang, Z.; Xu, K.; Wang, M.; Wang, H. Controlling Crystal Structures and Multiple Thermo- and Vapochromic Behaviors of Benzimidazole-Based Squaraine Dyes by Molecular Design and Solvent Adjustment. *Chem. Eur. J.* **2018**, *24*, 13205–13212. [[CrossRef](#)]
37. Li, L.; Ma, H.; Zhang, J.; Zhao, E.; Hao, J.; Huang, H.; Li, H.; Li, P.; Gu, X.; Tang, B.Z. Emission-Tunable Soft Porous Organic Crystal Based on Squaraine for Single-Crystal Analysis of Guest-Induced Gate-Opening Transformation. *J. Am. Chem. Soc.* **2021**, *143*, 3856–3864. [[CrossRef](#)]
38. Qiao, W.; Yao, P.; Chen, Y.; Xiao, Q.; Zhang, L.; Li, Z.A. Squaraine-based AIEgens for reversible mechanochromism, sensitive and selective hypochlorite detection and photostable far-red fluorescence cell imaging. *Mater. Chem. Front.* **2020**, *4*, 2688–2696. [[CrossRef](#)]

39. Qiao, W.; Ma, T.; Wang, S.; Li, L.; Liu, M.; Jiang, H.; Wu, Y.; Zhu, J.; Li, Z.A. Designing Squaraine Dyes with Bright Deep-Red Aggregation-Induced Emission for Specific and Ratiometric Fluorescent Detection of Hypochlorite. *Adv. Funct. Mater.* **2021**, *31*, 2105452. [[CrossRef](#)]
40. Yao, P.; Qiao, W.; Wang, Y.; Peng, H.; Xie, X.; Li, Z.A. Deep-red Emissive Squaraine-AIEgen in Elastomer Enabling High Contrast and Fast Thermoresponse for Anti-Counterfeiting and Temperature Sensing. *Chem. Eur. J.* **2022**, *28*, e202200725. [[CrossRef](#)]
41. Grande, V.; Shen, C.-A.; Deiana, M.; Dudek, M.; Olesiak-Banska, J.; Matczyszyn, K.; Würthner, F. Selective parallel G-quadruplex recognition by a NIR-to-NIR two-photon squaraine. *Chem. Sci.* **2018**, *9*, 8375–8381. [[CrossRef](#)] [[PubMed](#)]
42. Fan, X.; Zhang, D.; Li, H.; Sun, S.; Xu, Y. A BSA-squaraine hybrid system for selectively detecting Ag⁺ in absolute PBS and sequential construction of logic functions. *Sens. Actuators B Chem.* **2017**, *245*, 290–296. [[CrossRef](#)]
43. Wang, G.; Xu, W.; Guo, Y.; Fu, N. Near-infrared squaraine dye as a selective protein sensor based on self-assembly. *Sens. Actuators B Chem.* **2017**, *245*, 932–937. [[CrossRef](#)]
44. Xiong, L.; Ma, J.; Huang, Y.; Wang, Z.; Lu, Z. Highly Sensitive Squaraine-Based Water-Soluble Far-Red/Near-Infrared Chromofluorogenic Thiophenol Probe. *ACS Sens.* **2017**, *2*, 599–605. [[CrossRef](#)] [[PubMed](#)]
45. Xu, Y.; Li, B.; Han, P.; Sun, S.; Pang, Y. Near-infrared fluorescent detection of glutathione via reaction-promoted assembly of squaraine-analyte adducts. *Analyst* **2013**, *138*, 1004–1007. [[CrossRef](#)] [[PubMed](#)]
46. Grande, V.; Doria, F.; Freccero, M.; Würthner, F. An Aggregating Amphiphilic Squaraine: A Light-up Probe That Discriminates Parallel G-Quadruplexes. *Angew. Chem. Int. Ed.* **2017**, *56*, 7520–7524. [[CrossRef](#)]
47. Fam, K.T.; Collot, M.; Klymchenko, A.S. Probing biotin receptors in cancer cells with rationally designed fluorogenic squaraine dimers. *Chem. Sci.* **2020**, *11*, 8240–8248. [[CrossRef](#)]
48. Karpenko, I.A.; Collot, M.; Richert, L.; Valencia, C.; Villa, P.; Mély, Y.; Hibert, M.; Bonnet, D.; Klymchenko, A.S. Fluorogenic Squaraine Dimers with Polarity-Sensitive Folding as Bright Far-Red Probes for Background-Free Bioimaging. *J. Am. Chem. Soc.* **2015**, *137*, 405–412. [[CrossRef](#)]
49. Lin, Y.; Sun, L.; Zeng, F.; Wu, S. An Unsymmetrical Squaraine-Based Activatable Probe for Imaging Lymphatic Metastasis by Responding to Tumor Hypoxia with MSOT and Aggregation-Enhanced Fluorescent Imaging. *Chem. Eur. J.* **2019**, *25*, 16740–16747. [[CrossRef](#)]
50. Yang, X.; Yang, Z.; Wu, Z.; He, Y.; Shan, C.; Chai, P.; Ma, C.; Tian, M.; Teng, J.; Jin, D.; et al. Mitochondrial dynamics quantitatively revealed by STED nanoscopy with an enhanced squaraine variant probe. *Nat. Commun.* **2020**, *11*, 3699. [[CrossRef](#)]
51. Sreejith, S.; Joseph, J.; Lin, M.; Menon, N.V.; Borah, P.; Ng, H.J.; Loong, Y.X.; Kang, Y.; Yu, S.W.-K.; Zhao, Y. Near-Infrared Squaraine Dye Encapsulated Micelles for in Vivo Fluorescence and Photoacoustic Bimodal Imaging. *ACS Nano* **2015**, *9*, 5695–5704. [[CrossRef](#)] [[PubMed](#)]
52. Meador, W.E.; Autry, S.A.; Bessetti, R.N.; Gayton, J.N.; Flynt, A.S.; Hammer, N.I.; Delcamp, J.H. Water-Soluble NIR Absorbing and Emitting Indolizine Cyanine and Indolizine Squaraine Dyes for Biological Imaging. *J. Org. Chem.* **2020**, *85*, 4089–4095. [[CrossRef](#)] [[PubMed](#)]
53. Fukuda, T.; Yokomizo, S.; Casa, S.; Monaco, H.; Manganiello, S.; Wang, H.; Lv, X.; Ulumben, A.D.; Yang, C.; Kang, M.-W.; et al. Fast and Durable Intraoperative Near-infrared Imaging of Ovarian Cancer Using Ultrabright Squaraine Fluorophores. *Angew. Chem. Int. Ed.* **2022**, *61*, e202117330. [[CrossRef](#)] [[PubMed](#)]
54. Wu, I.C.; Yu, J.; Ye, F.; Rong, Y.; Gallina, M.E.; Fujimoto, B.S.; Zhang, Y.; Chan, Y.-H.; Sun, W.; Zhou, X.-H.; et al. Squaraine-Based Polymer Dots with Narrow, Bright Near-Infrared Fluorescence for Biological Applications. *J. Am. Chem. Soc.* **2015**, *137*, 173–178. [[CrossRef](#)]
55. Chen, L.; Wu, L.; Yu, J.; Kuo, C.T.; Jian, T.; Wu, I.C.; Rong, Y.; Chiu, D.T. Highly photostable wide-dynamic-range pH sensitive semiconducting polymer dots enabled by dendronizing the near-IR emitters. *Chem. Sci.* **2017**, *8*, 7236–7245. [[CrossRef](#)]
56. Peng, H.-Q.; Niu, L.-Y.; Chen, Y.-Z.; Wu, L.-Z.; Tung, C.-H.; Yang, Q.-Z. Biological Applications of Supramolecular Assemblies Designed for Excitation Energy Transfer. *Chem. Rev.* **2015**, *115*, 7502–7542. [[CrossRef](#)]
57. Wu, L.; Liu, J.; Li, P.; Tang, B.; James, T.D. Two-photon small-molecule fluorescence-based agents for sensing, imaging, and therapy within biological systems. *Chem. Soc. Rev.* **2021**, *50*, 702–734. [[CrossRef](#)]
58. Sun, C.-L.; Lv, S.-K.; Liu, Y.-P.; Liao, Q.; Zhang, H.-L.; Fu, H.; Yao, J. Benzoinidolic squaraine dyes with a large two-photon absorption cross-section. *J. Mater. Chem. C* **2017**, *5*, 1224–1230. [[CrossRef](#)]
59. Sun, C.-L.; Liao, Q.; Li, T.; Li, J.; Jiang, J.-Q.; Xu, Z.-Z.; Wang, X.-D.; Shen, R.; Bai, D.-C.; Wang, Q.; et al. Rational design of small indolic squaraine dyes with large two-photon absorption cross section. *Chem. Sci.* **2015**, *6*, 761–769. [[CrossRef](#)]
60. Chang, H.-J.; Bondar, M.V.; Liu, T.; Liu, X.; Singh, S.; Belfield, K.D.; Sheely, A.; Masunov, A.E.; Hagan, D.J.; Van Stryland, E.W. Electronic Nature of Neutral and Charged Two-Photon Absorbing Squaraines for Fluorescence Bioimaging Application. *ACS Omega* **2019**, *4*, 14669–14679. [[CrossRef](#)]
61. Gao, F.-P.; Lin, Y.-X.; Li, L.-L.; Liu, Y.; Mayerhöffer, U.; Spent, P.; Su, J.-G.; Li, J.-Y.; Würthner, F.; Wang, H. Supramolecular adducts of squaraine and protein for noninvasive tumor imaging and photothermal therapy in vivo. *Biomaterials* **2014**, *35*, 1004–1014. [[CrossRef](#)] [[PubMed](#)]
62. Yao, D.; Wang, Y.; Zou, R.; Bian, K.; Liu, P.; Shen, S.; Yang, W.; Zhang, B.; Wang, D. Molecular Engineered Squaraine Nanoprobe for NIR-II/Photoacoustic Imaging and Photothermal Therapy of Metastatic Breast Cancer. *ACS Appl. Mater. Interfaces* **2020**, *12*, 4276–4284. [[CrossRef](#)] [[PubMed](#)]

63. Wei, Y.; Hu, X.; Shen, L.; Jin, B.; Liu, X.; Tan, W.; Shangguan, D. Dicyanomethylene Substituted Benzothiazole Squaraines: The Efficiency of Photodynamic Therapy In Vitro and In Vivo. *eBioMedicine* **2017**, *23*, 25–33. [[CrossRef](#)]
64. Ji, C.; Gao, Q.; Dong, X.; Yin, W.; Gu, Z.; Gan, Z.; Zhao, Y.; Yin, M. A Size-Reducible Nanodrug with an Aggregation-Enhanced Photodynamic Effect for Deep Chemo-Photodynamic Therapy. *Angew. Chem. Int. Ed.* **2018**, *57*, 11384–11388. [[CrossRef](#)] [[PubMed](#)]
65. Lima, E.; Ferreira, O.; Gomes, V.S.D.; Santos, A.O.; Boto, R.E.; Fernandes, J.R.; Almeida, P.; Silvestre, S.M.; Reis, L.V. Synthesis and in vitro evaluation of the antitumoral phototherapeutic potential of squaraine cyanine dyes derived from indolenine. *Dyes Pigment.* **2019**, *167*, 98–108. [[CrossRef](#)]